energies

Article

Minimum Current Optimization of DBSRC Considering the Dead-Time Effect

Jiawen Yang, Yu Zhang * and Xinmi Wu

The State Key Laboratory of Advanced Electromagnetic Engineering and Technology, School of Electrical and Electronic Engineering, Huazhong University of Science and Technology, Wuhan 430074, China
* Correspondence: zyu1126@hust.edu.cn

Abstract: In a dual-bridge series resonant converter (DBSRC) working at a high switching frequency, the dead-time effect is a serious issue. When the minimum current trajectory (MCT) method is applied, the inductor current cannot be minimized due to the dead-time effect, and the range of the soft switching is reduced. Considering the dead-time, this paper first presents a theoretical analysis of the transmission power and the soft-switching characteristics based on the fundamental harmonic approximation (FHA) approach. Then, a minimum current trajectory method considering the dead-time (MCT-d) is proposed to achieve the minimum inductor current by compensating for the dead-time. This method can extend the soft-switching range as well. Finally, the experimental results validate the theoretical analysis and the improvement of the converter's efficiency.

Keywords: DC-DC converter; dead-time; phase-shift control; zero voltage switching; resonant converters; minimum current trajectory

Citation: Yang, J.; Zhang, Y.; Wu, X. Minimum Current Optimization of DBSRC Considering the Dead-Time Effect. *Energies* **2022**, *15*, 8484. https://doi.org/10.3390/en15228484

Academic Editor: Nicu Bizon

Received: 9 October 2022
Accepted: 12 November 2022
Published: 14 November 2022

1. Introduction

Dual active bridge (DAB) DC/DC converters have been widely applied in renewable energy, DC power distribution systems, electric vehicles, energy storage systems, and uninterruptible power supplies [1–8]. The topology of the dual-bridge series resonant converter (DBSRC) is shown in Figure 1. Through the resonance tank, the inductor current of the DBSRC is near a sinusoidal wave, and the soft-switching characteristic of the switches is better than that of a DAB [9–14].

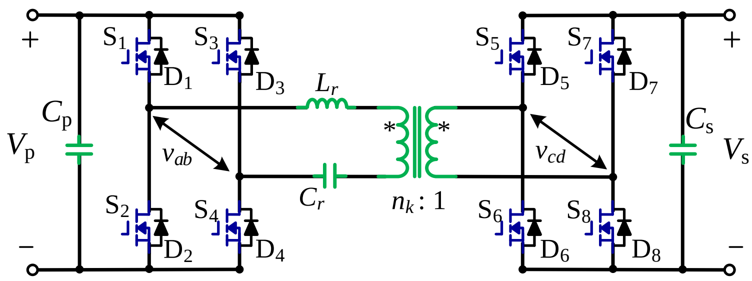

Figure 1. DBSRC topology.

The basic modulation of the DBSRC is single phase-shift (SPS) modulation [6]. However, under this modulation, the conduction losses and switching losses of the power switches cannot be minimized, which will significantly reduce the converter's efficiency [15]. In the DBSRC, extending the soft-switching range and reducing the inductor current are two key ways to significantly improve the efficiency [16,17]. Reducing the inductor current's root mean square (RMS) value can improve the efficiency more than by extending the soft-switching range [18–20]. Therefore, a minimum current trajectory (MCT) method based on extended phase-shift (EPS) was proposed to minimize the RMS value of the inductor current in the DBSRC, thus significantly improving the efficiency [10,20,21]. However, the dead-time effects were not considered.

In DABs, the effect of the dead-time cannot be negligible at a high switching frequency. The phenomena of the voltage polarity reversal and phase drift of the DAB, which is caused by dead-time, are reported in [22,23], and a power transfer model considering dead-time was proposed in [24,25], but only SPS was considered in these studies. The minimum dead-time to meet soft switching or safe operation was given in [26–28], but these studies focused on adjusting the dead-time. The authors of [29] concluded that the converter should be operated with less dead-time, but there is no comprehensive derivation on how to lower the dead-time. An improved TPS method is proposed in [30], but it only considers the case of low power boost and does not consider the optimization of current RMS.

In summary, the existing studies did not consider the dead-time effects on the current stress optimization and the soft switching of the DBSRC and did not propose any solution for the current stress minimization considering the dead-time within the full power range of the DBSRC.

This study used the fundamental harmonic approximation (FHA) method to analyze the working principle of the DBSRC [11]. Considering the dead-time effects on the transmission power and soft switching, a minimum current trajectory with dead-time (MCT-d) was proposed. The MCT-d compensates for transmission power deviation and extends the ZVS-on range under the influence of dead-time.

The paper is organized as follows. In Section 2, the working principles of the DBSRC and MCT optimization strategies are introduced. In Section 3, the effect of dead-time on the output voltage of the active bridge is analyzed in detail, and a dead-time compensation method for the minimum current RMS of the DBSRC is proposed. Experimental verification is carried out in Section 4 to illustrate the reliability of the experimental method. Finally, the conclusions are shown in Section 5.

2. Resonant Converter Control

2.1. DBSRC Fundamental Characteristics

In the DBSRC topology shown in Figure 1, the switches S_1–S_4 and their antiparallel diodes D_1–D_4 form the primary-side H-bridge, and switches S_5–S_8, with their antiparallel diodes D_5–D_8, form the secondary-side H-bridge. The two H-bridges are connected by a resonant tank and a high-frequency transformer with a voltage ratio of n_k. The switching frequency f_s is slightly larger than the resonant frequency f_r.

The control waveform of the DBSRC is exhibited in Figure 2, where d_1 and d_2 are the duty ratios of the primary and secondary H-bridge output voltages; φ is the phase-shift angle between the primary and secondary sides, and the sign of φ determines the direction of the transmitted power; and θ is the phase angle at which the resonant current lags behind the primary bridge voltage.

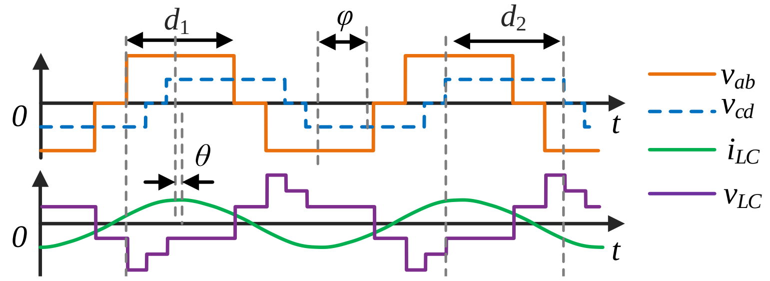

Figure 2. DBSRC voltage and current waveforms.

The primary- and secondary-side DC bus voltages are V_p and V_s, respectively, and the normalized voltage conversion ratio is $k = n_k V_s / V_p$. The periodicity time is $T_s = 1/f_s$, the half periodicity time is $T_{hs} = T_s/2$, the resonant frequency is $f_r = 1/(2\pi\sqrt{L_r C_r})$, and the switching resonant frequency ratio is $F_n = f_s/f_r$. The characteristic impedance is

$Z_r = \sqrt{L_r/C_r}$, and the dead-time is $T_d = d_d T_{hs}$. The following basic values were selected for Equation (1) to obtain Equation (1) in the normalized form [10,11]:

$$V_B = V_p\ ,\ Z_B = Z_r\ ,\ P_B = {V_B}^2/Z_B\ ,\ I_B = V_B/Z_B \tag{1}$$

In the subscript of the following variables, n denotes the Fourier decomposition coefficient of the n-th harmonic of the voltage. The voltage can be expressed as Equation (2):

$$\begin{aligned} v_{ab,pu}(t) &= \sum_{n=1,3,\cdots}^{+\infty} \tfrac{4}{n\pi} \cdot \cos[n\pi(1-d_1)/2] \sin(n\omega_s t) \\ v_{cd,pu}(t) &= \sum_{n=1,3,\cdots}^{+\infty} \tfrac{4k}{n\pi} \cdot \cos[n\pi(1-d_2)/2] \sin(n\omega_s t - n\varphi) \\ v_{LC,pu}(t) &= v_{ab,pu}(t) - v_{cd,pu}(t) \end{aligned} \tag{2}$$

The resonant tank impedance and current are given in Equation (3):

$$\begin{aligned} & X_{LC,pu} = \sum_{n=1,3,\cdots}^{+\infty} [nF_n - 1/(nF_n)] \\ & i_{LC,pu}(t) = \sum_{n=1,3,\cdots}^{+\infty} \tfrac{v_{ab,n,pu}(t) - v_{cd,n,pu}(t)}{X_{LC,n,pu}(t)} = \sum_{n=1,3,\cdots}^{+\infty} \tfrac{2\sqrt{{A_n}^2 + {B_n}^2}}{(n^2F_n - 1/F_n)\pi} [\, \sin(n\omega_s t + \theta_n)] \\ & where \\ & A_n = k\sin(n\pi d_2/2)\sin(n\varphi),\ B_n = k\sin(n\pi d_2/2)\cos(n\varphi) - \sin(n\pi d_1/2),\ \theta_n = \arctan(B_n/A_n) \end{aligned} \tag{3}$$

The phase of the fundamental component of the inductor current can be approximated by Equation (4):

$$\theta \approx \theta_1 = \arctan\left[\frac{k\sin(\pi d_2/2)\cos(\varphi) - \sin(\pi d_1/2)}{k\sin(\pi d_2/2)\sin(\varphi)}\right] \tag{4}$$

According to Equations (2) and (3), the transmitted power can be expressed as:

$$P_o = \frac{1}{2\pi}\sum_{n=1,3,\cdots}^{+\infty}\int_0^{2\pi} v_{ab,n,pu}(t) i_{LC,n,pu}(t) d(\omega_s t) = \frac{4k}{\pi^2}\sum_{n=1,3,\cdots}^{+\infty}\frac{\sin(n\pi d_1/2)\sin(n\pi d_2/2)\sin(n\varphi)}{n(n^2F_n - 1/F_n)} \tag{5}$$

The theoretical maximum transmission power (P_{max}) can be approximated by the maximum transmission power of the fundamental wave as given by Equation (6):

$$P_{max} = \frac{4k}{\pi^2}\frac{1}{(F_n - 1/F_n)} \tag{6}$$

The normalized transmission power is $p_0 = P_o/P_{max}$. In open loop control, p_0 will be directly given, and in closed loop control, p_0 will be calculated by the PI controller. Further, the values of the three control degrees of freedom—d_1, d_2, and φ—can be calculated according to p_0.

Equation (3) indicates that the resonant tank equivalent impedance increases rapidly at high frequencies, and the high-frequency inductor current decays rapidly. As a result, the high-frequency harmonic of both the current and the transmitted power of the DBSRC is small. In fact, due to the resonance of the inductor and capacitor, the resonant current and voltage are close to sinusoidal, and the resonant converters can be analyzed and designed using an AC equivalent circuit, as shown in Figure 3.

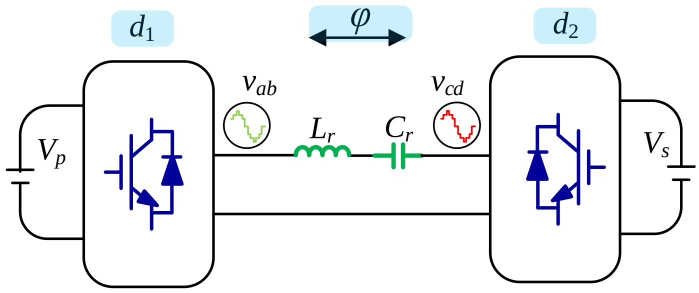

Figure 3. DBSRC AC equivalent circuits.

2.2. Inductor Current Minimization of DBSRC

A small resonant current can reduce switching losses, on-state losses, and magnetic losses, thus improving the efficiency. The optimization method of the MCT is shown in Figure 4.

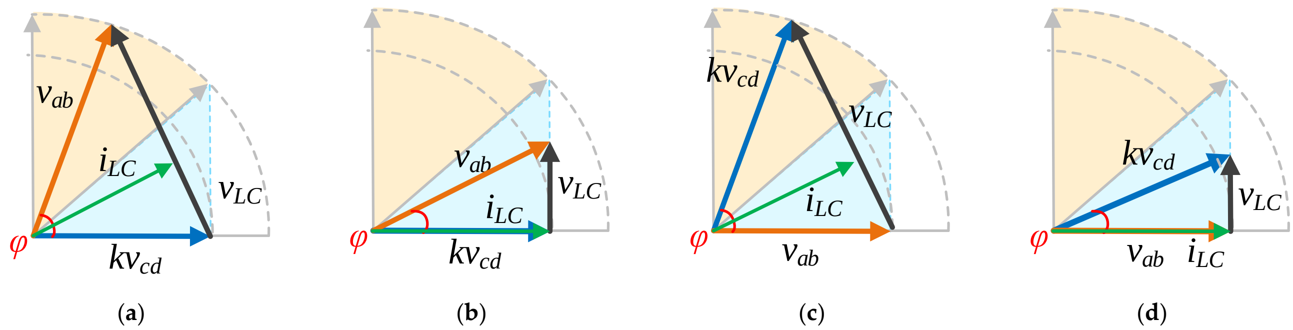

Figure 4. MCT optimization strategy: (**a**) $k < 1$, $p_0 > p_{MCT}$; (**b**) $k < 1$, $p_0 < p_{MCT}$; (**c**) $k > 1$, $p_0 > p_{MCT}$; (**d**) $k > 1$, $p_0 < p_{MCT}$.

If $k < 1$ and the transmitted power $p_0 > p_{MCT}$, the primary- and secondary-side duty ratios, $d_{1,}$ and d_2, are set to 1. This is equivalent to the single-phase-shift modulation, which can control the transmitted power according to the phase-shift angle φ. As shown in Figure 4a, the resonant tank current phase lags the primary-side voltage and is ahead of the secondary-side voltage. In this state, when the device is turned on, the current is negative and will flow through the antiparallel diode, so ZVS on can be realized.

If $k < 1$ and the transmitted power $p_0 < p_{MCT}$, the secondary-side duty ratio, d_2, is set to 1. As shown in Figure 4b, the inductor current is in the phase with the secondary-side voltage, lagging the primary voltage. The secondary-side devices can be turned on soft. The primary-side devices are turned on hard because d_1 is not 1, and the current of the devices has passed zero before the device is turned on. The phase difference between the resonant tank voltage and the secondary-side voltage is 90°. Therefore, the RMS value of the resonant tank current is the minimum, and the reactive power on the secondary side is zero.

When $k \geq 1$, d_1, d_2, and φ have a similar relationship to $k < 1$.

Ideally, when $p_0 > p_{MCT}$, all switching devices can achieve ZVS switching, and when $p_0 < p_{MCT}$, at least half of the switching devices can achieve soft switching. The p_{MCT} should satisfy Equation (7). The expressions of the duty cycle and the phase-shift angle can be found in Table 1.

$$if(k<1):\ \begin{cases}\cos\varphi_{MCT}=\frac{k\sin(\pi d_2/2)}{\sin(\pi d_1/2)}=k\\ p_{MCT}=\sin\varphi_{MCT}\end{cases}\qquad if(k\geq 1):\ \begin{cases}\cos\varphi_{MCT}=\frac{\sin(\pi d_1/2)}{k\sin(\pi d_2/2)}=\frac{1}{k}\\ p_{MCT}=\sin\varphi_{MCT}\end{cases} \tag{7}$$

Table 1. MCT phase-shift angle and duty cycle.

	$p_0 < p_{MCT}$	$p_0 \geq p_{MCT}$	p_{MCT}
$k < 1$	$\begin{cases} d_1 = \frac{2}{\pi}\arcsin\left(\sqrt{{p_0}^2 + k^2}\right) \\ d_2 = 1 \\ \varphi = \arctan(p_0/k) \end{cases}$	$\begin{cases} d_1 = 1 \\ d_2 = 1 \\ \varphi = \arcsin(p_0) \end{cases}$	$p_{MCT} = \sqrt{1 - k^2}$
$k \geq 1$	$\begin{cases} d_1 = 1 \\ d_2 = \frac{2}{\pi}\arcsin\left(\sqrt{{p_0}^2 + (1/k)^2}\right) \\ \varphi = \arctan(kp_0) \end{cases}$	$\begin{cases} d_1 = 1 \\ d_2 = 1 \\ \varphi = \arcsin(p_0) \end{cases}$	$p_{MCT} = \sqrt{1 - (1/k)^2}$

In practical applications, the switching frequency in the DBSRC is high. Therefore, the dead-time cannot be negligible. A significant difference between the duty cycle and its theoretical value can be observed, which significantly impacts the transmitted power. Meanwhile, the results of the MCT show a deviation, which is analyzed in the following section.

3. Dead-Time Effect and Its Compensation under MCT

3.1. Effect of Dead-Time on the Half-Bridge Output Voltage

Considering a half-bridge consisting of S_1 and S_2, the bridge's output voltages under different switching states are analyzed in this paper. The conclusions obtained from the half-bridge are also valid for other multilevel half-bridge topologies (e.g., three-level half-bridge).

In a half-bridge, the current paths under different switching states are shown in Figure 5. The blue current path is denoted as negative, and the red current path is denoted as positive. When S_1 or S_2 is turned on, the voltage at point O is independent of the current direction. However, during the dead-time, both S_1 and S_2 are turned off. When the current flows out of point O, the voltage at point O is V_P, and when the current flows into point O, the voltage at point O is V_N. The direction of the current determines the output voltage at point O.

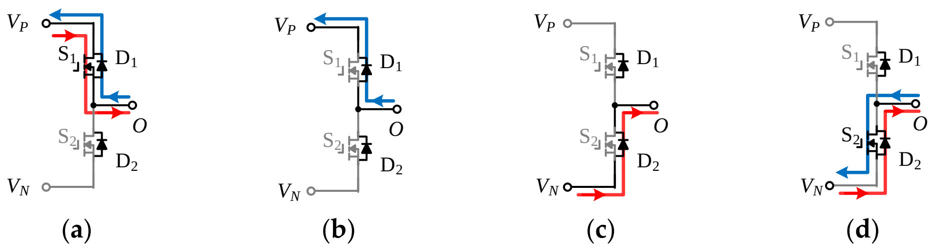

Figure 5. Voltage and current paths in various switching states in a half (H)-bridge: (**a**) current path A; (**b**) current path B; (**c**) current path C; (**d**) current path D.

Figure 6 shows the possible O-point potentials during the period when S_1 is turned off and S_2 is turned on after dead-time. Different combinations of current paths will result in different effects on both the soft-switching and O-point output voltages, as shown in Table 2. As can be seen in Table 2, considering the output voltage, the dead-time has no effect on the output voltage under Mode A; the output voltage waveforms under Mode B are affected by the dead-time. The output voltage waveforms under Modes C and D are also affected by the dead-time, but the effect is smaller compared to Mode B. For switching losses, there is one hard-switching turn-on in Modes A and B. The switching actions in Modes C and D occur near the current crossing zero point, and the switching losses are both small. Overall, the switching losses and dead-time under Modes A, C, and D have a more negligible effect on the output voltage. In contrast, the dead-time under Mode B has a significant effect.

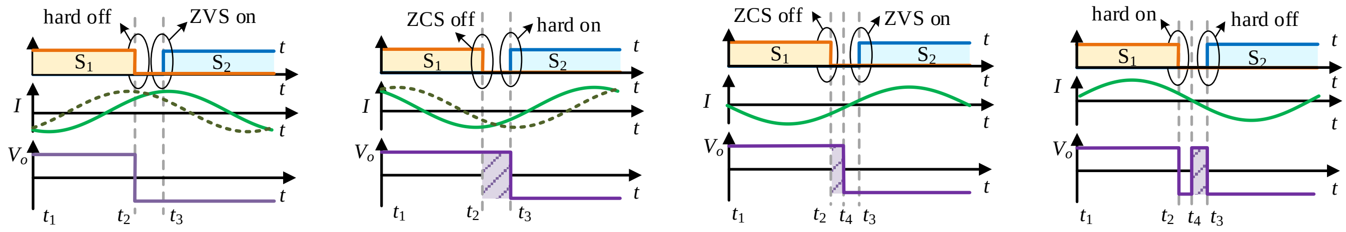

(**a**) (**b**) (**c**) (**d**)

Figure 6. Drive, current, and voltage waveforms considering dead-time: (**a**) Mode A; (**b**) Mode B; (**c**) Mode C; (**d**) Mode D.

Table 2. Effects of different current conditions on half-bridge soft switching and output voltage during dead-time.

Mode in Figure 6	S_1 (off)	S_2 (on)	Current Paths in Figure 5	On/Off Losses	Influence of Output Voltage
A	hard	soft	a-c-d	medium	none
B	soft	hard	a-b-d	medium	heavy
C	soft	soft	a-b-c-d	light	medium
D	hard	hard	a-c-b-d	heavy	medium

3.2. Effect of Dead-Time on Power Loss under MCT Strategy

In Section 3.1, the dead-time effects on the half-bridge output voltage and soft switching were analyzed. When the DBSRC adopts an MCT control scheme, due to the influence of the dead-time, the actual output open-loop transmission power (p_{open}) will be inconsistent with the expected value p_0, and the specific corresponding relationship is shown in Figure 7. In order to illustrate the trend and limit the condition of the dead-time affecting the transmission power, Figure 7 shows the influence of the p_{open} when d_d increases from 0 to 0.4. It can be seen that the larger the d_d, the more serious the influence of the dead-time. The power closed-loop control can compensate for the deviation of the open-loop transmission power caused by the dead-time. However, the RMS value of the inductor current will no longer be the minimum value, and the losses will increase. Here, we analyze in detail the open-loop control of the transmitted power and the closed-loop control of the current's RMS of the MCT control strategy under the influence of dead-time.

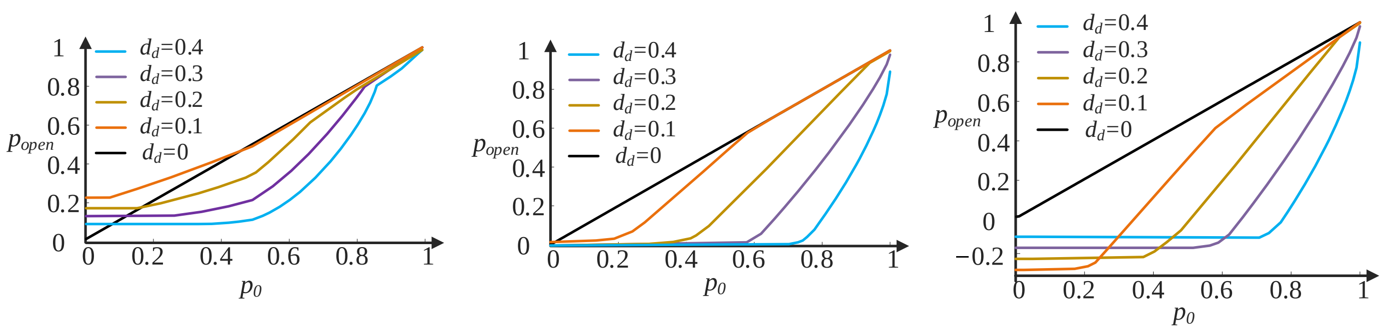

(**a**) (**b**) (**c**)

Figure 7. Effects of dead-time on SRC open-loop control of transmission power under an MCT control strategy: (**a**) $k < 1$; (**b**) $k = 1$; (**c**) $k > 1$.

3.2.1. The Effect of Dead-Time on the Full Power Range under Open-Loop Control

With the MCT control scheme, the impact of the dead-time on the DBSRC appears in Figure 6 in Modes A, B, C, and D. As shown in Figure 8b, the DBSRC may have four dead-time impact states, when $k < 1$, the sequence from a light load to a heavy load is Mode

B–D–A, and when $k > 1$, the sequence from a light load to a heavy load is Mode B–C–A–D. The flow chart for judging the different states is shown in the Figure 8a.

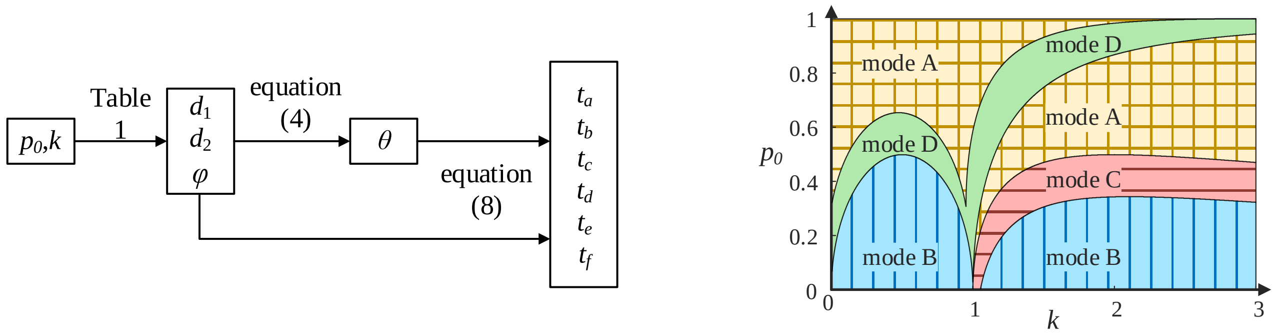

(**a**) (**b**)

Figure 8. Influence of dead-time on the full power range of the MCT: (**a**) calculation flow chart; (**b**) dead-time impact range.

The influence of the dead-time on the DBSRC under a light load appears in Mode B, and the transmission power and current RMS will be seriously affected. As the load gradually increases, the DBSRC starts to operate in Modes C and D, where the dead-time also impacts the transmission power, but the impact is more negligible than in Mode B. The dead-time under the heavy load affects Mode A, while the transmission power and soft switching are not affected.

The voltage and current waveforms of the DBSRC from a light load to a heavy load for $k < 1$ and $k \geq 1$ are shown in Figure 9, where t_a is the moment when the resonant tank current crosses zero from negative to positive; t_b is the switch-off moment when the primary-side voltage jumps from the zero level to the positive level; t_c is the moment when t_b switches after a dead-time; t_d is the moment when the resonant tank current crosses zero from positive to negative; t_e is the switch-off moment when the primary-side voltage jumps from the zero level to the positive output level; t_f is the moment when t_e switches after a dead-time. The corresponding relationship between t_a to t_f and the different modes in Figure 8b can be obtained from Table 3. t_a–t_f can be expressed as in Equation(8):

$$\begin{cases} t_a = T_{hs}\theta/\pi \\ t_b = (-d_1/2)T_{hs} + T_{hs}/2 \\ t_c = (d_d - d_1/2)T_{hs} + T_{hs}/2 \end{cases} \quad \begin{cases} t_d = T_{hs}\theta/\pi + T_{hs} \\ t_e = (d + d_2/2)T_{hs} + T_{hs}/2 \\ t_d = (d_d + d + d_2/2)T_{hs} + T_{hs}/2 \end{cases} \tag{8}$$

Table 3. Correspondence between voltage and current phases and dead-time effects.

$k < 1$	$t_a < t_b$ Mode B	$t_b \leq t_a < t_c$ Mode D	$t_c \leq t_a$ Mode A
$k \geq 1$	$t_d < t_e$ Mode A	$t_e \leq t_d < t_f$ Mode C	$t_f \leq t_d$ Mode B

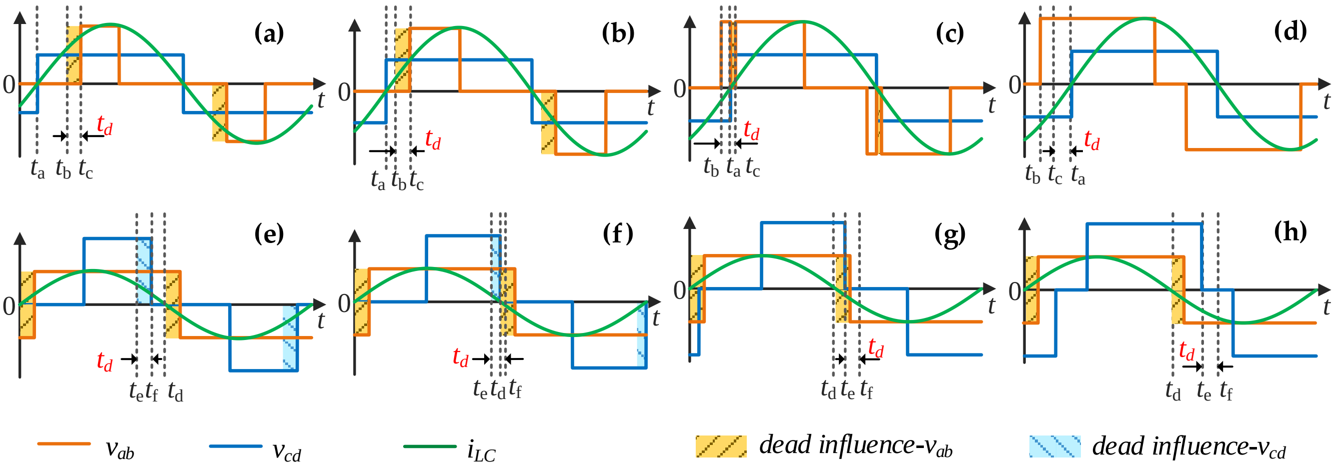

Figure 9. Inductor current and output voltage waveforms under MCT: (**a**) $k = 0.5$, $p_0 = 0.2$; (**b**) $k = 0.5$, $p_0 = 0.4$; (**c**) $k = 0.5$, $p_0 = 0.6$; (**d**) $k = 0.5$, $p_0 = 0.8$; (**e**) $k = 2$, $p_0 = 0.2$; (**f**) $k = 2$, $p_0 = 0.4$; (**g**) $k = 2$, $p_0 = 0.6$; (**h**) $k = 2$, $p_0 = 0.8$.

3.2.2. Effect of Dead-Time on RMS Current and Soft Switching under Closed-Loop Control

The effect of the dead-time on the transmitted power is mainly focused on the dead-time in Mode B, so we mainly analyzed the effect of Mode B on the MCT control.

When $k < 1$, the dead-time causes the actual duty cycle of the primary output voltage v_{ab} to decrease from d_1 to $d_1 - d_\mathrm{d}$, and the actual inter-bridge phase shift φ decreases to $\varphi - d_d\pi/2$. At this time, the open-loop transfer power can be expressed as Equation (9). When $k \geq 1$, the dead-time causes the actual duty cycle of the secondary output voltage v_{cd} to increase from d1 to $d_2 + d_d$, and the actual inter-bridge phase shift φ decreases to $\varphi - d_d\pi/2$. At this time, the open-loop transfer power can be expressed as Equation (10).

$$p_b = \left[\frac{\sqrt{1 - p_0{}^2 - k^2}}{\sqrt{p_0{}^2 + k^2}} \sin\left(\frac{\pi d_d}{2}\right) + \cos\left(\frac{\pi d_d}{2}\right)\right]\left[p_0 \cos\left(\frac{\pi d_d}{2}\right) + k \sin\left(\frac{\pi d_d}{2}\right)\right] \tag{9}$$

$$p_f = \left[\frac{\sqrt{k^2 - k^2 p_0{}^2 - 1}}{\sqrt{p_0{}^2 k^2 + 1}} \sin\left(\frac{\pi d_d}{2}\right) + \cos\left(\frac{\pi d_d}{2}\right)\right]\left[p_0 \cos\left(\frac{\pi d_d}{2}\right) - \frac{1}{k} \sin\left(\frac{\pi d_d}{2}\right)\right] \tag{10}$$

The effect of the dead-time on the high-frequency voltage, the phase-shift angle, and the transmitted power under open-loop control is shown in Table 4. The closed-loop control can solve the problem of insufficient transmission power. However, at this time, the voltage and current phase are still affected by the dead-time, resulting in an increase in the resonant tank current for the same active power output. In Figure 10c,g, it can be seen that the closed-loop power regulation can make the DBSRC output the desired transmission active power. However, the current phase distortion caused by the dead-time still exists, generating reactive power and increasing the RMS value of the resonant current, reducing the efficiency.

Table 4. Effect of dead-time on RMS, phase shift, and transmission power.

	v_{ab} RMS	v_{cd} RMS	Phase Shift	Standardized Transmission Power
$k < 1$, with dead-time	$\sin(\pi d_1/2)$	1	φ	p_0
$k < 1$, without dead-time	$\sin(\pi d_1/2 - \pi d_\mathrm{d}/2)$	1	$\varphi_b = \varphi - \pi d_d/2$	p_b in Equation (9)
$k \geq 1$, with dead-time	1	$\sin(\pi d_2/2)$	φ	p_0
$k \geq 1$, without dead-time	1	$\sin(\pi d_2/2 + \pi d_d/2)$	$\varphi_f = \varphi - \pi d_d/2$	p_f in Equation (10)

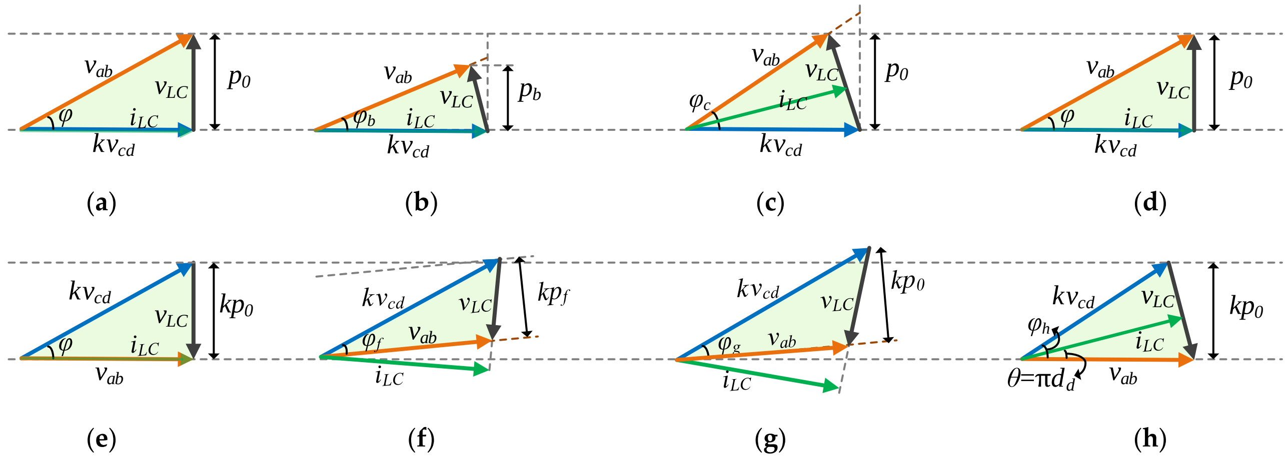

Figure 10. Effect of dead-time on MCT: (**a**) $k < 1$, MCT, without dead-time influence; (**b**) $k < 1$, with dead-time influence, open-loop control; (**c**) $k < 1$, MCT, with dead-time influence, close-loop control; (**d**) $k < 1$, MCT-d, with dead-time influence, close-loop control; (**e**) $k > 1$, MCT, without dead-time influence (**f**) $k > 1$, with dead-time influence, open-loop control; (**g**) $k > 1$, with dead-time influence, closed-loop control; (**h**) $k > 1$, MCT-d, with dead-time influence, closed-loop control.

According to the above analysis, the dead-time affects the high-frequency voltage phase and RMS value, affecting the transmitted power and the soft-switching range of the DBSRC. Therefore, a compensation method is proposed and described in the next section.

3.3. Minimum Current Trajectory with Dead-Time (MCT-d)

To address the impact of the dead-time on the MCT control scheme, it is necessary to reconsider the vector relationship of the high-frequency voltage and current while adding dead-time compensation to the drive signal. Three degrees of freedom, d_1, d_2, and φ, can be recalculated accordingly to achieve the minimum current RMS optimization scheme with dead-time compensation.

When $k < 1$, compensating for the loss of the v_{ab} duty cycle can compensate for the effect of dead-time on the transmitted power. The v_{ab} can be compensated by modifying the primary-side part of the switching signal to operate in advance of the T_d time. Figure 11a demonstrates the drive signal compensation. By the dead-time, the duty ratios of v_{ab} and v_{cd} decrease to $d_1{}' = d_1 - d_d$ and $d_2{}' = d_2 - d_d$. Therefore, the turn-on time of S_1 and S_2 must change from t_1 and t_2 to $t_1{}'$ $t_2{}'$. The vector triangle achieves the minimum current RMS state at this point, as shown in Figure 10d.

Compensating for the loss of the v_{ab} duty cycle can compensate for the effect of the dead-time on the transmitted power. The v_{ab} can be compensated for by modifying the primary-side part of the switching signal to operate in advance of the $d_d T_{hs}$ time. Figure 11a demonstrates the drive signal compensation. By the dead-time, the duty ratios of v_{ab} and v_{cd} decreased to $d_1{}' = d_1 - d_d$ and $d_2{}' = d_2 - d_d$. Therefore, the turn-on time of S_1 and S_2 must change from t_1 and t_2 to $t_1{}'$ and $t_2{}'$. The minimum current RMS state is achieved at this point, as shown in Figure 10d.

When $k > 1$, the situation is more complicated. To shorten the high-level voltage duration of V_P and V_N, S_7 and S_8 must be turned on from t_6 and t_7 to $t_6{}'$ and $t_7{}'$. Suppose the primary-side voltage and resonant current are in phase. In this case, the primary-side bridge outputs a high level when the current is positive and a low level when the current is negative during the dead-time. This does not match the actual relationship between the current and the output voltage during the dead-time.

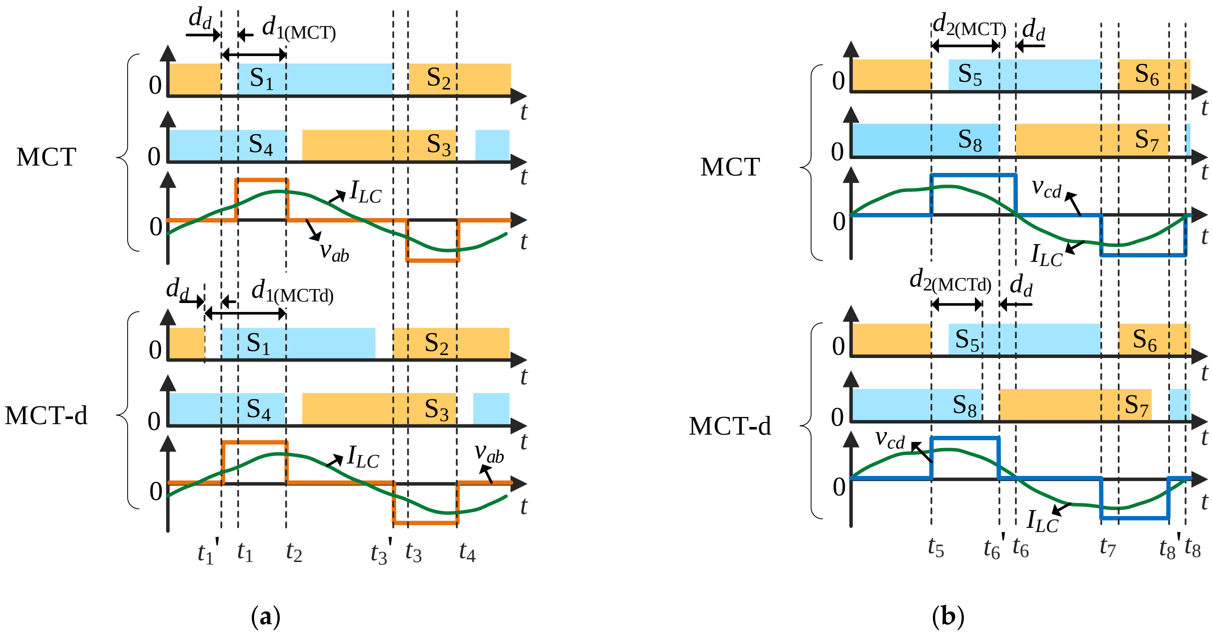

Figure 11. Drive compensation: (**a**) $k < 1$, primary H-bridge; (**b**) $k \geq 1$, secondary H-bridge.

Therefore, although the theoretical analysis without considering the dead-time effect can achieve the same phase of the primary-side voltage and resonant current, the actual waveform affected by the dead-time in the primary-side voltage and resonant current must have a phase difference, and the absolute value of this phase difference is at least $d_d\pi$. The primary-side device is in the hard on mode when the current is ahead of v_{ab}. When the current is lagging behind v_{ab}, the primary-side device is in the soft on mode. Adjusting the voltage and current phase so that the current i_L lags behind the voltage v_{ab} by an angle of πd_d can reduce the number of hard turn-ons. The new vector triangle at this point is shown in Figure 10h. In Figure 10, it can be seen that the currents in Figure 10f,g,h are at a certain angle to the primary-side voltage. The current in Figure 10f,g is ahead of the primary-side voltage, and there is a hard turn-on. After the phase adjustment, the current in Figure 10g lags behind the primary-side voltage, which is a soft turn-on.

In order to achieve the minimum current RMS control under the influence of the dead-time effect, the new control parameters, φ, d_1, and d_2, under MCT-d can be recalculated according to Table 5, where θ can be recalculated according to Figure 8a under MCT.

Table 5. MCT-d phase-shift angle and duty cycle.

	$p_0 < p_{MCT\text{-}d}$	$p_0 \geq p_{MCT\text{-}d}$	$p_{MCT\text{-}d}$
$k < 1$	$\begin{cases} d_1 = \frac{2}{\pi}\arcsin\left(\sqrt{{p_0}^2 + k^2}\right) + d_d \\ d_2 = 1 \\ \varphi = \arctan\left(\frac{p_0}{k}\right) + \frac{d_d}{2}\pi \end{cases}$	$\begin{cases} d_1 = 1 \\ d_2 = 1 \\ \varphi = \arcsin p_0 \end{cases}$	$\sqrt{1-k^2}$
$k \geq 1$	$\begin{cases} d_1 = 1 \\ d_2 = \frac{2}{\pi}\arcsin\sqrt{{p_0}^2 + (k - p_0\tan\theta)^2} - d_d \\ \varphi = \arctan\frac{p_0}{k\sin(\pi/2 - p_0\tan\theta)} - \frac{d_d}{2}\pi \end{cases}$	$\begin{cases} d_1 = 1 \\ d_2 = 1 \\ \varphi = \arcsin p_0 \end{cases}$	$\frac{-\tan\theta + \sqrt{k^2\tan^2\theta - 1}}{k + k\tan^2\theta}$

3.4. Comparison of MCT-d and MCT Optimization Effect

When the same power is transmitted, the MCT-d reduces the current RMS compared to the MCT control strategy. At the same time, the MCT-d also has an advantage over the MCT in ZVS soft switching.

According to the open-loop transmitted power shown in Equations (9) and (10), the d_1, d_2, and φ needed for the closed-loop power regulation under MCT can be obtained correspondingly. Thus, the resonant current i_{LC} under the closed-loop control can be calculated. The current RMS optimization is shown in Figure 12. When $k < 1$, the current RMS value of the MCT-d is lower than that of the MCT, and when $k > 1$, the difference between the RMS currents of the MCT-d and the MCT is small. The larger the dead-time, the more the current RMS value is affected.

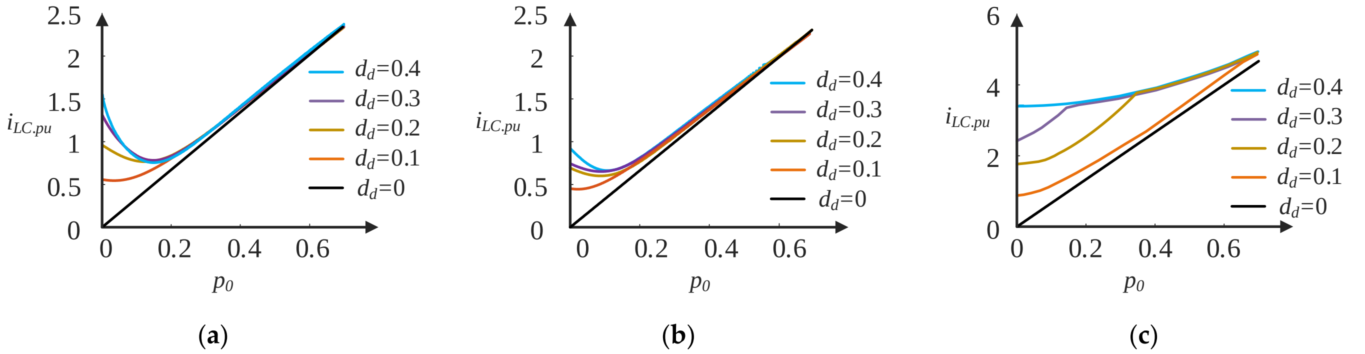

Figure 12. Comparison of current RMS values at different dead-times: (**a**) k = 0.5; (**b**) k = 0.75; (**c**) k = 2.

The MCT-d control strategy also extends the ZVS on the range. Figure 13 shows the soft-switching cases with the MCT control strategy and the MCT-d control strategy. Figure 13a shows the primary-side switching losses using the MCT scheme, Figure 13b shows the primary-side switching losses for the MCT-d scheme, and Figure 13c shows the secondary-side switching losses for the MCT and MCT-d schemes. It can be seen that with the MCT-d scheme, the ZVS range of the primary-side switching device is extended. At the same time, there is no effect on the soft-switching range of the secondary-side switching device. The green part of Figure 13 shows the current crossing zero during the dead-time, and the primary-side bridge is in the hard on and hard off modes at a dead-time. However, at this time, the switching process is near the current crossing zero point, and the primary-side switching losses are not significant.

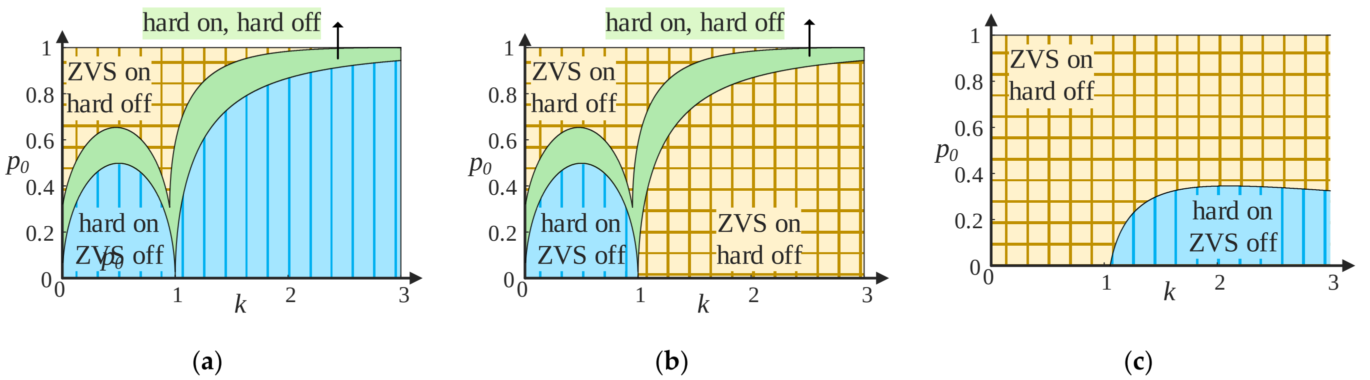

Figure 13. ZVS range: (**a**) MCT, primary-side switches; (**b**) MCT-d, primary-side switches; (**c**) MCT and MCT-d, secondary-side switches.

4. Simulation and Experiment

To verify the proposed optimization method, a MATLAB/Simulink simulation and an experimental prototype were built according to the parameters shown in Table 6. The experimental prototype is shown in Figure 14.

Table 6. Experimental prototype parameters.

Parameter	Value	Parameter	Value
V_{dc1}	100–200 V	L_r	174 µH
V_{dc2}	100–200 V	C_r	110 nF
n_k	1	dead-time	1 µs
f_s	40 *k*Hz	P_o	2 *k*W

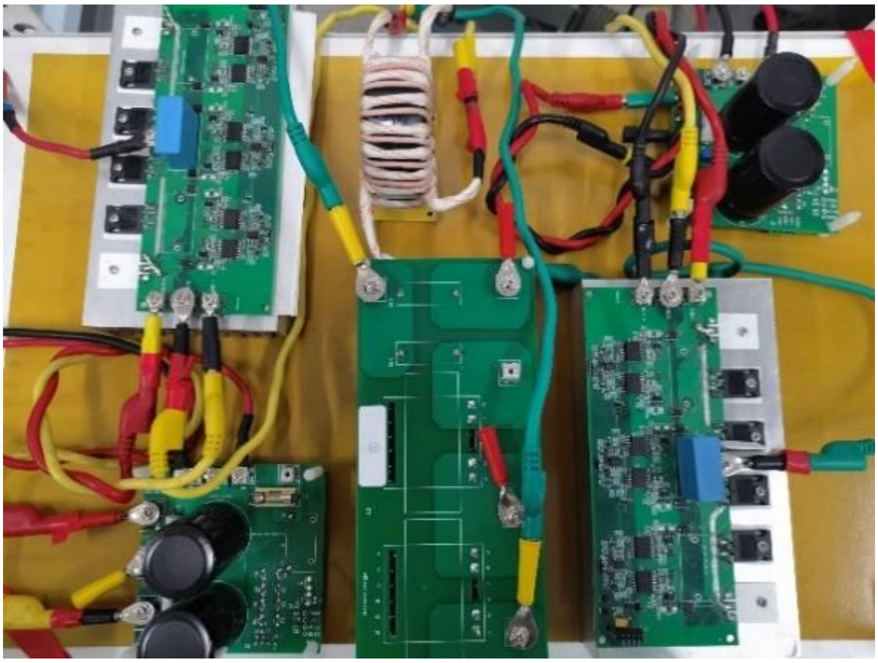

Figure 14. Experimental prototype (2 *k*W).

4.1. Current RMS Result

The simulated current RMS waveforms for k = 0.5 and k = 2 are shown in Figure 15. For k < 1, the current RMS of the MCT-d control strategy was smaller than that for the MCT, especially under a light load. For k > 1, the difference between the current RMS of the two control strategies was small, mainly in the switching losses of the primary-side devices.

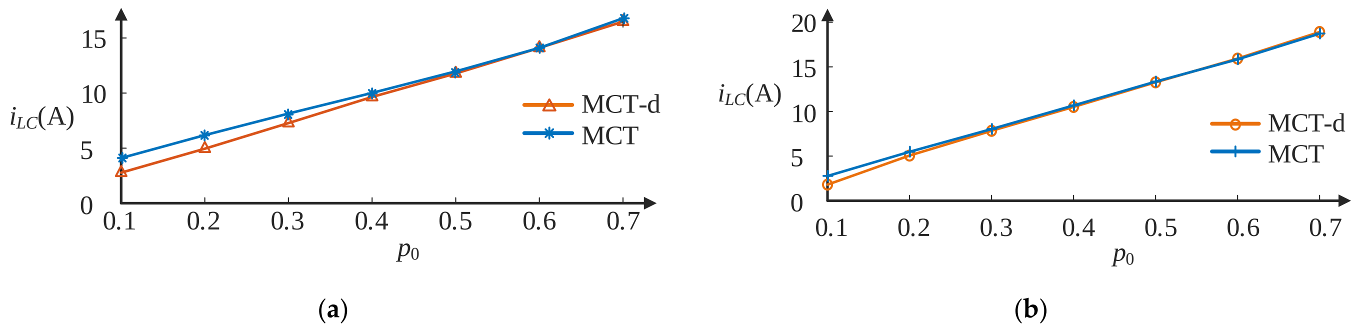

Figure 15. Current RMS simulation, dd = 0.1 Ths: (**a**) k = 0.5; (**b**) k = 2.

Using closed-loop power control, the voltage and current waveforms at p_0 = 0.3 and p_0 = 0.6 are shown in Figures 16 and 17. Figure 16 shows the light load working condition. At this time, the resonant tank current in the MCT-d optimization scheme was smaller, and the waveform was closer to the sine. Figure 17 shows the heavy load working condition. At this time, the resonant tank currents of the two schemes were similar, and the optimization effect was relatively insignificant.

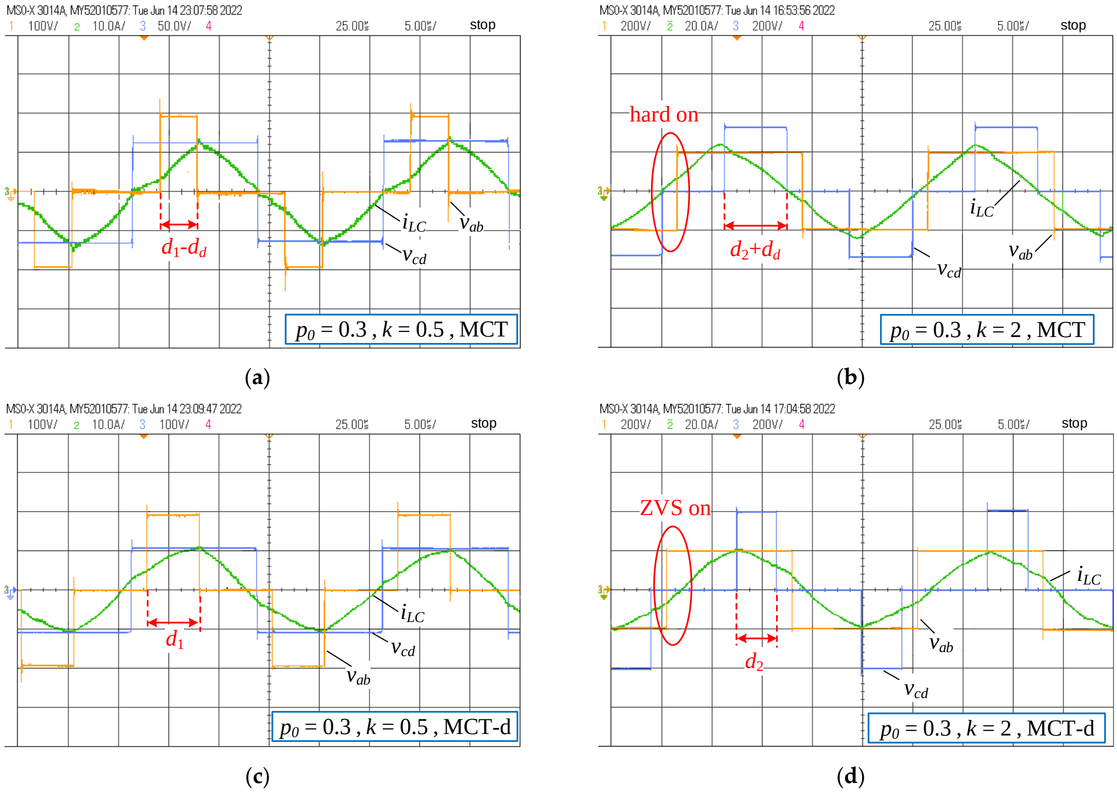

Figure 16. p_0 = 0.3 correction for soft switching and loss of voltage duty cycle: (**a**) k = 0.5, MCT; (**b**) k = 2, MCT; (**c**) k = 0.5, MCT-d; (**d**) k = 2, MCT-d.

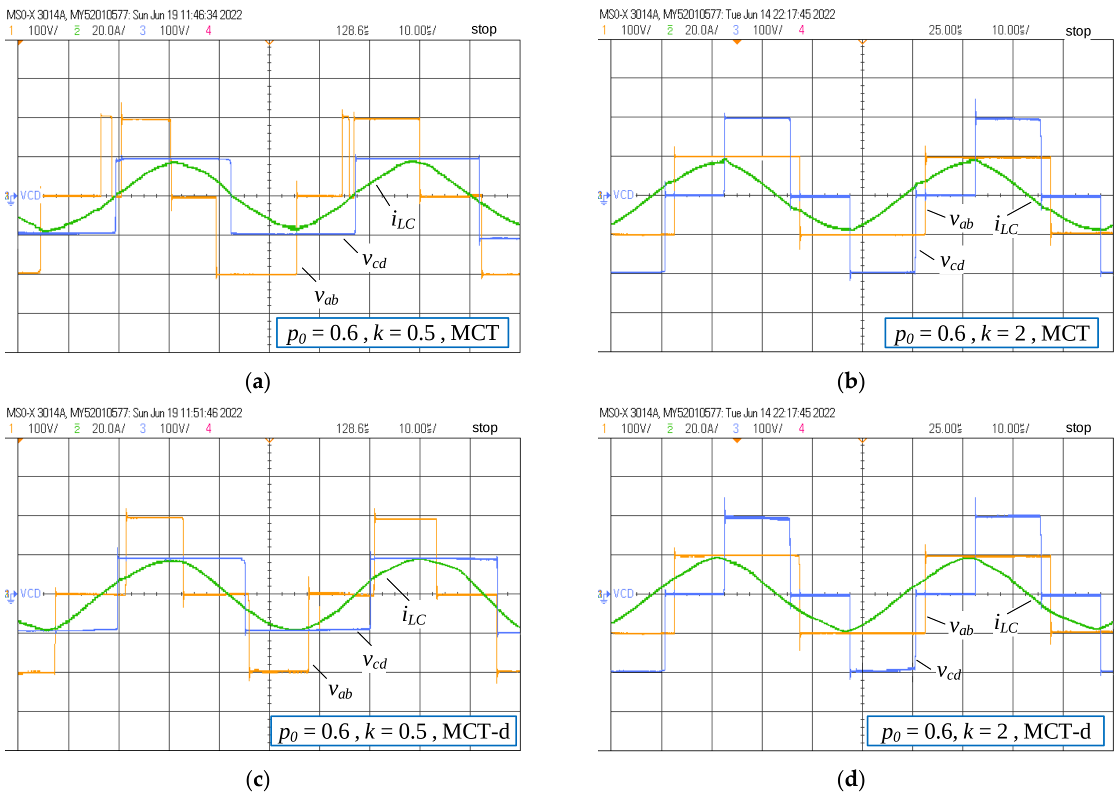

Figure 17. p_0 = 0.6 correction for soft switching and loss of voltage duty cycle: (**a**) k = 0.5, MCT; (**b**) k = 2, MCT; (**c**) k = 0.5, MCT-d; (**d**) k = 2, MCT-d.

4.2. Soft-Switching Comparison under a Light Load

Figure 16 also reflects the soft switch optimization of MCT-d. Consistent with the previous analysis, the MCT-d scheme under light load can expand the soft-switching range. When $k > 1$, the MCT-d avoided the hard switching due to the dead-time. Meanwhile, a better soft-switching characteristic than that of the MCT was achieved.

4.3. MCT and MCT-d Efficiency Curve

Figure 18 shows the efficiency of the MCT-d. The efficiency under a light load was significantly improved compared to that of the MCT. However, the optimization effect was not apparent under a heavy load. This efficiency result is consistent with that of MCT in soft switching and current RMS optimization.

This is because the p_0, d_1, d_2, and φ under light load are small, which will be close to d_d, and DBSRC will be seriously affected by the dead-time. In essence, the MCT-d scheme aims to compensate for the efficiency reduction caused by dead-time. Therefore, MCT-d works better under light load conditions that are more affected by dead-time. Under heavy load conditions, the dead-time has relatively little impact, and the efficiency improvement of MCT-d compared with MCT is limited.

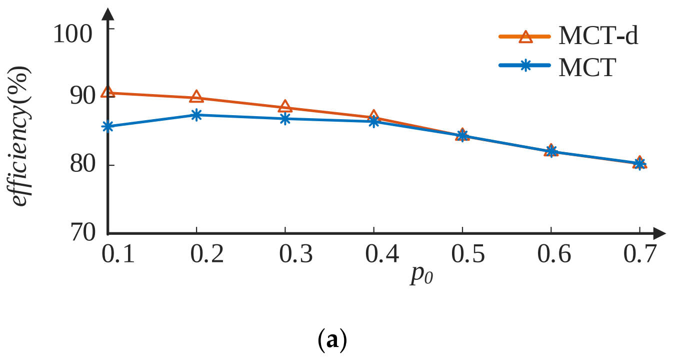

Figure 18. Efficiency results: (**a**) $k = 0.5$; (**b**) $k = 2$.

5. Conclusions

This paper details the dead-time's effects on the transmission power and soft-switching characteristics based on the fundamental wave approximation method. Due to the dead-time effect, the current minimization of the actual inductor cannot be ensured when applying the traditional MCT method. This paper proposed an MCT-d method to eliminate the dead-time effect. The MCT-d method minimized the tank current and extended the soft-switching range, and the proposed method could reduce the switching losses and improve the efficiency when the voltage ratio deviated from 1. Finally, the experimental results validated the theoretical analysis.

Author Contributions: Conceptualization, J.Y. and Y.Z.; methodology, J.Y. and Y.Z.; software, J.Y., Y.Z. and X.W.; validation, J.Y. and Y.Z.; formal analysis, J.Y. and Y.Z.; investigation, J.Y. and Y.Z.; resources, J.Y. and Y.Z.; data curation, J.Y. and Y.Z.; writing—original draft preparation, J.Y.; writing—review and editing, Y.Z.; visualization, J.Y.; supervision, Y.Z.; project administration, Y.Z.; funding acquisition, Y.Z. All authors have read and agreed to the published version of the manuscript.

Funding: This work was supported by the National Natural Science Foundation of China under Grant No. 51977092.

Data Availability Statement: Not applicable.

Conflicts of Interest: The authors declare no conflict of interest.

References

1. De Doncker, R.W.A.A.; Divan, D.M.; Kheraluwala, M.H. A Three-Phase Soft-Switched High-Power-Density DC/DC Converter for High-Power Applications. *IEEE Trans. Ind. Appl.* **1991**, *27*, 63–73. [CrossRef]
2. Kheraluwala, M.N.; Gascoigne, R.W.; Divan, D.M.; Baumann, E.D. Performance Characterization of a High-Power Dual Active Bridge DC-to-DC Converter. *IEEE Trans. Ind. Appl.* **1992**, *28*, 1294–1301. [CrossRef]
3. Inoue, S.; Akagi, H. A Bidirectional Isolated DC–DC Converter as a Core Circuit of the Next-Generation Medium-Voltage Power Conversion System. *IEEE Trans. Power Electron.* **2007**, *22*, 535–542. [CrossRef]
4. Shigenori, I.; Hirofumi, A. A Bidirectional DC–DC Converter for an Energy Storage System with Galvanic Isolation. *IEEE Trans. Power Electron.* **2007**, *22*, 2299–2306. [CrossRef]
5. Oggier, G.G.; GarcÍa, G.O.; Oliva, A.R. Switching Control Strategy to Minimize Dual Active Bridge Converter Losses. *IEEE Trans. Power Electron.* **2009**, *24*, 1826–1838. [CrossRef]
6. Zhao, B.; Song, Q.; Liu, W.; Sun, Y. Overview of Dual-Active-Bridge Isolated Bidirectional DC–DC Converter for High-Frequency-Link Power-Conversion System. *IEEE Trans. Power Electron.* **2014**, *29*, 4091–4106. [CrossRef]
7. Zhao, B.; Song, Q.; Liu, W. Efficiency Characterization and Optimization of Isolated Bidirectional DC–DC Converter Based on Dual-Phase-Shift Control for DC Distribution Application. *IEEE Trans. Power Electron.* **2013**, *28*, 1711–1727. [CrossRef]
8. Shao, S.; Chen, L.; Shan, Z.; Gao, F.; Chen, H.; Sha, D.; Dragičević, T. Modeling and Advanced Control of Dual-Active-Bridge DC–DC Converters: A Review. *IEEE Trans. Power Electron.* **2022**, *37*, 1524–1547. [CrossRef]
9. Krismer, F.; Biela, J.; Kolar, J.W. A Comparative Evaluation of Isolated Bi-Directional DC/DC Converters with Wide Input and Output Voltage Range. In Proceedings of the Fourtieth IAS Annual Meeting. Conference Record of the 2005 Industry Applications Conference, Hong Kong, China, 2–6 October 2005; IEEE: Hong Kong, China, 2005; Volume 1, pp. 599–606.
10. Luca, C.; Daniel, S.; Douglas, B.; Regan, Z.; Dragan, M.; Boris, J. Minimum Current Operation of Bidirectional Dual-Bridge Series Resonant DC/DC Converters. *IEEE Trans. Power Electron.* **2012**, *27*, 3266–3276. [CrossRef]
11. Li, X.; Bhat Ashoka, K.S. Analysis and Design of High-Frequency Isolated Dual-Bridge Series Resonant DC/DC Converter. *IEEE Trans. Power Electron.* **2010**, *25*, 850–862. [CrossRef]
12. Robert, L.; Florian, M.; De Doncker Rik, W. Comparison of Non-Resonant and Super-Resonant Dual-Active ZVS-Operated High-Power DC-DC Converters. In Proceedings of the 2009 13th European Conference on Power Electronics and Applications, Barcelona, Spain, 8–10 September 2009; pp. 1–10.
13. Yang, B.; Ge, Q.; Zhao, L.; Zhou, Z. Analysis and Comparison of High Power Bidirectional Isolated DC/DC Converters for Power Electronic Transformer. In Proceedings of the 2018 21st International Conference on Electrical Machines and Systems (ICEMS), Jeju, Korea, 7–10 October 2018; pp. 2465–2470.
14. Bez, F.; Han, W.; Corradini, L. A Low-Complexity Trajectory Controller for Reduced Conduction Losses in Series-Resonant Dual Half-Bridge Converters. *IEEE Trans. Power Electron.* **2018**, *33*, 9963–9974. [CrossRef]
15. Bai, H.; Chris, M. Eliminate Reactive Power and Increase System Efficiency of Isolated Bidirectional Dual-Active-Bridge DC–DC Converters Using Novel Dual-Phase-Shift Control. *IEEE Trans. Power Electron.* **2008**, *23*, 2905–2914. [CrossRef]
16. Han, W.; Corradini, L. General Closed-Form ZVS Analysis of Dual-Bridge Series Resonant DC–DC Converters. *IEEE Trans. Power Electron.* **2019**, *34*, 9289–9302. [CrossRef]
17. Waffler, S.; Kolar, J.W. A Novel Low-Loss Modulation Strategy for High-Power Bidirectional Buck + Boost Converters. *IEEE Trans. Power Electron.* **2009**, *24*, 1589–1599. [CrossRef]
18. Zhao, B.; Yu, Q.; Leng, Z.; Chen, X. Switched Z-Source Isolated Bidirectional DC–DC Converter and Its Phase-Shifting Shoot-Through Bivariate Coordinated Control Strategy. *IEEE Trans. Ind. Electron.* **2012**, *59*, 4657–4670. [CrossRef]
19. Hou, N.; Song, W.; Wu, M. Minimum-Current-Stress Scheme of Dual Active Bridge DC–DC Converter with Unified Phase-Shift Control. *IEEE Trans. Power Electron.* **2016**, *31*, 8552–8561. [CrossRef]
20. Yaqoob, M.; Loo, K.H.; Lai, Y.M. Extension of Soft-Switching Region of Dual-Active-Bridge Converter by a Tunable Resonant Tank. *IEEE Trans. Power Electron.* **2017**, *32*, 9093–9104. [CrossRef]
21. Choi, W.; Rho, K.-M.; Cho, B.-H. Fundamental Duty Modulation of Dual-Active-Bridge Converter for Wide-Range Operation. *IEEE Trans. Power Electron.* **2016**, *31*, 4048–4064. [CrossRef]
22. Bai, H.; Mi, C.C.; Gargies, S. The Short-Time-Scale Transient Processes in High-Voltage and High-Power Isolated Bidirectional DC–DC Converters. *IEEE Trans. Power Electron.* **2008**, *23*, 2648–2656. [CrossRef]
23. Kadavelugu, A.; Baek, S.; Dutta, S.; Bhattacharya, S.; Das, M.; Agarwal, A.; Scofield, J. High-Frequency Design Considerations of Dual Active Bridge 1200 V SiC MOSFET DC-DC Converter. In Proceedings of the 2011 Twenty-Sixth Annual IEEE Applied Power Electronics Conference and Exposition (APEC), Fort Worth, TX, USA, 6–11 March 2011; pp. 314–320.
24. Zhao, B.; Song, Q.; Liu, W.; Sun, Y. Dead-Time Effect of the High-Frequency Isolated Bidirectional Full-Bridge DC–DC Converter: Comprehensive Theoretical Analysis and Experimental Verification. *IEEE Trans. Power Electron.* **2014**, *29*, 1667–1680. [CrossRef]
25. Xie, Y.; Sun, J.; Freudenberg, J.S. Power Flow Characterization of a Bidirectional Galvanically Isolated High-Power DC/DC Converter Over a Wide Operating Range. *IEEE Trans. Power Electron.* **2010**, *25*, 54–66. [CrossRef]
26. Li, J.; Chen, Z.; Shen, Z.; Mattavelli, P.; Liu, J.; Boroyevich, D. An Adaptive Dead-Time Control Scheme for High-Switching-Frequency Dual-Active-Bridge Converter. In Proceedings of the 2012 Twenty-Seventh Annual IEEE Applied Power Electronics Conference and Exposition (APEC), Orlando, FL, USA, 19–23 March 2012; pp. 1355–1361.

27. Yaqoob, M.; Loo, K.H.; Lai, Y.M. Modeling the Effect of Dead-Time on the Soft-Switching Characteristic of Variable-Frequency Modulated Series-Resonant DAB Converter. In Proceedings of the 2017 IEEE 18th Workshop on Control and Modeling for Power Electronics (COMPEL), Stanford, CA, USA, 9–12 July 2017; pp. 1–8.
28. Teng, J.-H.; Liu, B.-H. Three-Stage Dead-Time Adjustment Scheme for Conversion Efficiency Enhancement of Phase-Shift Full-Bridge Converters at Light Loads. *IEEE Trans. Ind. Electron.* **2021**, *68*, 1210–1219. [CrossRef]
29. Song, C.; Chen, A.; Chen, J.; Du, C.; Zhang, C. Dead-Time Effect Analysis of Dual Active Bridge DC-DC Converter with Dual-Phase-Shift Control. In Proceedings of the 2017 Chinese Automation Congress (CAC), Jinan, China, 20–22 October 2017; pp. 6545–6550.
30. Jin, X.; Kong, L.; Deng, Z.; Li, H.; Gong, L.; Wang, Y. Improved Triple-Phase-Shift Control for DAB Converter to Minimize Current Stress with All-ZVS Operation Considering Dead-Time Effect. In Proceedings of the 2021 IEEE 12th Energy Conversion Congress Exposition-Asia (ECCE-Asia), Singapore, 24–27 May 2021; pp. 373–378.